Research Article

Effect of the Precipitating Agent on the Synthesis and Sintering Behavior of 20 mol% Sm-Doped Ceria

Luca Spiridigliozzi,[1] Gianfranco Dell'Agli,[1,2] Mattia Biesuz,[3] Vincenzo M. Sglavo,[2,3] and Michele Pansini[1,2]

[1]*Department of Civil and Mechanical Engineering, University of Cassino and Southern Lazio,*
Via G. Di Biasio 43, 03043 Cassino, Italy
[2]*National Interuniversity Consortium of Materials Science and Technology (INSTM), Via G. Giusti 9, 50121 Florence, Italy*
[3]*Department of Industrial Engineering, University of Trento, Via Sommarive 9, 38123 Trento, Italy*

Correspondence should be addressed to Gianfranco Dell'Agli; dellagli@unicas.it

Nanocrystalline 20 mol% samaria-doped ceria powders ($Ce_{0.8}Sm_{0.2}O_{1.9}$) were synthesized by coprecipitation techniques using various precipitating agents in aqueous solution: ammonia, ammonium carbonate, tetramethylammonium hydroxide, and urea. The synthesized powders after calcination at 600°C possess a fluorite structure with nanometric size although they are characterized by a very different morphology and degree of agglomeration. Remarkable differences appear in the sintering behavior, especially because of the presence of hard agglomerates. The precipitating agent has therefore a crucial role in the coprecipitation process, which influences the morphology of the powders and in turn the sintering behavior. The obtained results clearly reveal that ammonium carbonate and urea are the best precipitating agents to obtain final dense products after sintering.

1. Introduction

Ceria (CeO_2) based ceramic materials have attracted much interest in many applications such as chemical-mechanical polishing media, automobile exhaust catalysts and supports, dense ceramic membranes for oxygen separation, low-temperature water-gas shift (WGS) reactions, and oxygen sensors [1]. A preeminent role is occupied by rare-earth-doped ceria used as electrolyte in IT-SOFC, that is, cells operating in the intermediate temperature range (500–700°C) [2–5]. In fact, the decrease of the operating temperature in SOFC is a very important goal for reducing interfacial reactions between cell components, mechanical and thermal degradation, and thermal expansion mismatch [6]. Ceria doped with aliovalent cation such as rare earth (RE^{+3}) has been found to be one of the most promising routes [7]. The oxygen vacancy concentration and the concomitant ion conductivity of ceria can be, in fact, increased significantly by the substitution of lower-valence rare earth RE^{+3} ion for Ce^{4+}. Gd^{+3} and Sm^{+3} cations are typically preferred because their ionic radius is very close to Ce^{4+} and this induces larger ionic conductivity [8]. A further and essential requisite for a ceramic electrolyte in SOFC is the densification and the absence of interconnected porosity. Nevertheless, one of the main drawbacks of ceria-based materials is the high temperature required for obtaining dense bodies. Traditional sintering routes require high temperature and long duration to induce full densification [9, 10]. An alternative and innovative possibility is the use of flash sintering [11] that allows us to produce very dense ceria-based ceramics at limited temperature under the effect of an electric field. An additional possibility is the synthesis of reactive, ultrafine, and nonagglomerated powders, which are densified at lower temperature. It is well known that chemical techniques allow us to prepare ceramic powders characterized by high purity, high homogeneity, and ultrafine size [12]. Among these, precipitation is probably the simpler and cheaper method to prepare ultrafine reactive powders. Nevertheless,

the sintering behavior of coprecipitated powders depends also on the used precipitating agent.

In the present work, 20% Sm-doped ceria was synthesized by a coprecipitation route, using four different coprecipitating agents: NH_3, tetramethylammonium hydroxide (TMAH), $(NH_4)_2CO_3$, and urea. Using the same synthesis conditions for coprecipitation, different powder morphology and, above all, different sintering behavior were pointed out.

2. Materials and Methods

Cerium (III) nitrate [$Ce(NO_3)_3 \cdot 6H_2O$ 99.0% Carlo Erba, Italy] and samarium nitrate [$Sm(NO_3)_3 \cdot 6H_2O$ 99.9% Carlo Erba, Italy] were used as starting materials for the synthesis of hydrous cerium-samarium oxide by coprecipitation with anhydrous composition $Ce_{0.8}Sm_{0.2}O_{1.90}$. The selected precipitating agents were ammonia solution [NH_3 solution 30%, Carlo Erba, Italy], TMAH [$(CH_3)_4NOH$ 10% w aqueous solution, Acros Organics, Italy], ammonium carbonate [$(NH_4)_2CO_3$ Reagent Grade J.T. Baker, The Netherlands], and urea [$CO(NH_2)_2$ 99.5% Carlo Erba, Italy]; they were used in concentrated aqueous solution in order to have 2 M nominal concentration during the coprecipitation. The proper amount of cerium and samarium salts was dissolved in deionized water to obtain a total cationic concentration equal to 0.1 M; the solution was then vigorously stirred for 1 h. With the exception of urea, the coprecipitation was carried out adding the precipitating agent-containing solution to that containing dissolved cerium and samarium under vigorous stirring; the solution was then aged for 1 h under stirring. When urea was used, it was dissolved in nitrates solution so that its concentration was 2 M. Upon heating at temperature in excess to 83°C, urea decomposes with the active and homogeneous release within the solution of OH^- and CO_3^{2-} ions that account for slow and homogeneous pH increase responsible for the coprecipitate formation avoiding the localized reactants distribution. In order to allow the complete coprecipitation, also in this case a 1 h ageing at about 90°C was realized. At the end of each synthesis, the coprecipitates were filtered, washed several times with deionized water, and dried overnight at 80°C. In the following, samples prepared by coprecipitation with NH_3, TMAH, $(NH_4)_2CO_3$, and urea will be indicated as N-SDC20, T-SDC20, C-SDC20, and U-SDC20, respectively.

The synthesized powders were calcined at 600°C for 2 h under static air atmosphere to induce complete crystallization of fluorite structure and eliminate the volatile species. The obtained powders were ground by hand using agata mortar and pestle.

The powders were compacted into cylindrical pellets by uniaxial pressing. Sintering was carried out in air at 1500°C for 6 h; heating rate of 5°C/min was used.

All samples were characterized by X-ray powder diffraction (XRD) using a Panalytical X'PERT MPD diffractometer to detect the crystalline phases. The primary crystallite size was calculated by the Scherrer equation [13]:

$$d = \frac{K\lambda}{B\cos(\theta)}, \tag{1}$$

where K is the shape factor equal to 0.89 for spherical particles, λ the X-ray wavelength (0.1541 nm for $CuK\alpha_1$), θ Bragg's angle of the cubic ceria (111) peak, and B the full width at half maximum (FWHM) of the (111) peak corrected for the instrumental broadening. B is calculated as

$$B = B_{sample} - B_{instr}, \tag{2}$$

where B_{instr} is determined using standard polycrystalline silicon. Both fitting profile, made using the pseudo-Voigt function as a mathematical model for the XRD peaks, and the calculations related to the Scherrer formula were carried out using the software X'Pert HighScore from Panalytical.

The specific surface area was measured by nitrogen adsorption technique through the BET method using a Micromeritics Gemini apparatus; the sample was preliminary dried under vacuum at 100°C.

The thermal behavior of the samples was studied by simultaneous differential scanning calorimetry and thermogravimetric analysis (DSC and TGA, Thermoanalyzer STA 409, Netzsch) in air using heating rate of 10°C/min up to 1200°C and using α-Al_2O_3 as a reference.

Dilatometric analyses were carried out in a dilatometer Linseis L75 using heating rate of 10°C/min up to 1550°C (piston load 200 mN). The samples, used for dilatometric tests, were shaped in cylindrical pellets ($\phi = 6$ mm, $t = 2.5$–3.0 mm) by uniaxial pressing at 200 MPa.

The apparent density of the sintered pellets was measured using a hydrostatic balance (Archimedes' principle).

The morphology of the synthesized powders and the microstructure of the sintered pellets were observed by scanning electron microscopy (SEM, Philips XL30) after carefully polishing one of the flat surfaces and successive chemical etching using nitric and fluoroboric acid solution.

3. Results and Discussion

The XRD patterns of the coprecipitates are reported in Figure 1. Different coprecipitates are actually formed: U-SDC20 is a well-crystallized material and N-SDC20 and T-SDC20 are constituted by poorly crystallized fluorite ceria while C-SDC20 is amorphous. This result is not surprising; it is well known that the particles obtained by precipitation can be amorphous or crystalline and the factors influencing the final structure are not clear yet [14].

U-SDC20 powder consists of a crystalline oxycarbonate-based phase, the diffraction pattern in Figure 1(d) corresponding to cerium oxide carbonate hydrate, $Ce_2O(CO_3)_2 \cdot H_2O$, reference pattern ICDD card n. 43-602; nevertheless, in this case a mixed cerium-samarium oxide carbonate hydrate is very likely formed, responsible for a clear shift of XRD peaks. This is confirmed by thermal behavior reported in Figure 2(d) where a pronounced and sharp endothermic peak associated with the oxycarbonate-based phase thermal decomposition occurs at 339°C. Such decomposition occurs with about 20% weight loss, which well agrees with the theoretical value (21%) corresponding to

the evolution of carbon dioxide and water and formation of fluorite phase, according to the global reaction:

$$(Ce_{0.8}, Sm_{0.2})_2 O (CO_3)_2 \cdot H_2O + 0.4O_2$$
$$\longrightarrow 2Ce_{0.8}Sm_{0.2}O_{1.90} + 2CO_2 + H_2O \qquad (3)$$
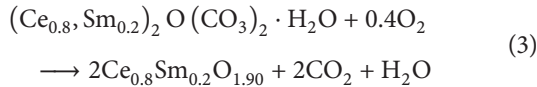
N-SDC20 and T-SDC20 specimens are partially amorphous and partially crystalline (fluorite structure of ceria), similar to gadolinium doped ceria coprecipitates reported in previous works [5, 10, 11]. XRD peaks (Figure 1 (a and b) for N-SDC20 and T-SDC20, resp.) appear always very broad, pointing out a very small crystal size, around 4 nm. A more careful inspection of XRD patterns reveals that the crystallization is slightly more pronounced in sample N-SDC20: XRD peak corresponding to (200) crystalline plane (at about $2\theta = 32°$) is practically absent in Figure 1(b) whereas it is clearly present in Figure 1(a). Therefore, although N-SDC20 and T-SDC20 are similar, the amorphous content in the latter is very probably larger. The corresponding thermographs, reported in Figures 2(a) and 2(b), confirm the XRD observations: the DSC curves reveal for both samples an exothermic peak associated with the crystallization of the amorphous phase, wide at 298°C and very sharp at 344°C for N-SDC20 and T-SDC20, respectively. In addition, TG curves indicate a weight loss of about 15.5% and 20.4% for N-SDC20 and T-SDC20, respectively. For ceria-based systems the formation of crystalline CeO_2 (theoretically without any weight loss) starts already at 0°C [15] whereas, when $Ce(OH)_4$ (with 17.3% as weight loss) is produced, it is amorphous [16]. It can be argued that, in the present ceria-based systems, formed by amorphous and crystalline fluorite phases, the larger the weight loss, the more abundant the amorphous content. This can be confirmed here because, assuming that the absorbed water amount is very similar between N-SDC20 and T-SDC20, as clearly shown in the thermographs (Figures 2(a) and 2(b)), the weight loss for T-SDC20, containing probably a larger amount of amorphous phase, is bigger, and vice versa for N-SDC20.

A further different behavior is observed for sample C-SDC20. In such case, a completely amorphous material is formed (see Figure 1(c)), characterized by a large weight loss, in excess to 33% (Figure 2(c)). According to previous results [17], in the present case a possible product of the precipitation with ammonium carbonate could be $(Ce_{0.8}Sm_{0.2})OHCO_3 \cdot 2.0H_2O$ whose total weight loss is 34.0%, in very good agreement with the weight loss associated with the thermograph in Figure 2(c). At a first approximation, about one-half of the total weight loss corresponds to the release of absorbed moisture and crystal water and is associated with the endothermic peak at 150°C; the remaining is accounted for by a decomposition reaction revealed by the endothermic peak at 419°C.

Finally, as shown in Figure 2, it is clear that all thermal transformations are completed at 600°C in all samples. For this reason, we selected this temperature for calcination to compare the effect of the different precipitating agents.

As expected, with a calcination at 600°C for 2 h, all phase transformations and complete crystallization in the fluorite Sm-doped ceria occurred in the various samples. XRD patterns reported in Figure 3 show that all peaks are attributable
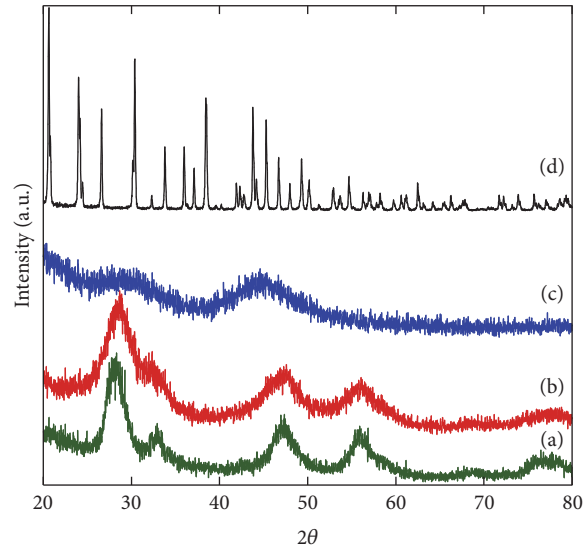

FIGURE 1: XRD patterns of the as-synthesized powders: N-SDC20 (a), T-SDC20 (b), C-SDC20 (c), and U-SDC20 (d).

TABLE 1: Cell parameters and crystal size of the calcined samples.

Sample	Cell parameter (nm)	Crystallite size (nm)
N-SDC20	0.5451	11
T-SDC20	0.5434	5
C-SDC20	0.5435	13
U-SDC20	0.5428	18

to fluorite ceria. Nevertheless, the analysis of the peaks shape points out that T-SDC20 does not appear well crystallized probably because of its very small crystal size, whereas U-SDC20 and C-SDC20 are both perfectly crystallized. N-SDC20 shows an intermediate behavior. Cell parameter determined according to the least squares procedure reported in [18] and crystal size calculated by (1) are reported in Table 1. The cell parameter appears in good agreement with the literature value (0.5433 nm as for ICDD reference patterns n. 75-158) for all samples and for the well-crystallized specimens (C-SDC20 and U-SDC20) the agreement is excellent. The calculated crystal size is nanometric for all samples although grain growth which occurred during the calcination step for T-SDC20 is nearly negligible.

It is well known [19–22] that upon coprecipitation the powder can form agglomerates, soft or hard. The properties, shape, and dimension of the granules are indeed related to the precipitation agent used for the synthesis. The morphology of the different calcined powders produced here was studied by SEM and some of the recorded micrographs are reported in Figure 4. It is possible to observe the very different clusters shape. In particular, the morphology of U-SDC20 powder (Figure 4(d)) is very homogeneous consisting of cubic-like particles, whose size is in the range 500 nm–1 μm, corresponding to clusters of nanometric-sized crystallites.
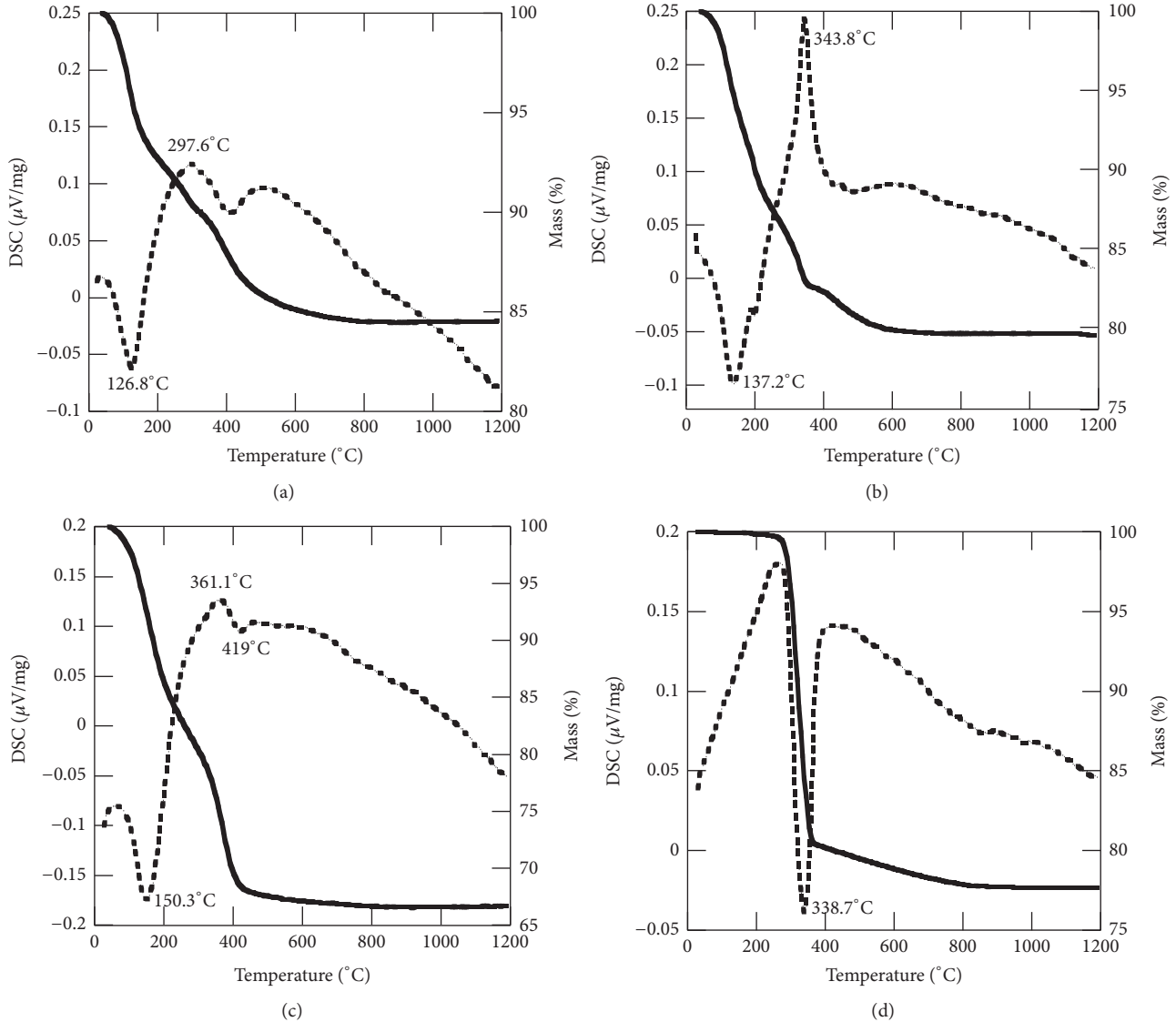
Figure 2: DSC (dashed lines) and TG (solid lines) thermographs of the as-synthesized powders: N-SDC20 (a), T-SDC20 (b), C-SDC20 (c), and U-SDC20 (d).

The specific surface area (S) of this sample can be correlated with the mean particles diameter by the relationship:

$$D = \frac{6}{(\rho S)},\qquad(4)$$

where ρ is the real material density (7.148 g/cm^3 as reported in ICDD card n. 75.158); both S and D are reported in Table 2.

For U-SDC20 powder, the obtained value is in perfect agreement with XRD crystal size reported in Table 1. The morphology of N-SDC20 and T-SDC20 specimens, shown in Figures 4(a) and 4(b), is similar and it is characterized by a broad distribution of particles size (there are very compact particles of several μm along with particles of less than 1 μm) with very irregular shape. Clearly, the compaction of such powders is difficult and the resulting green density is very low, also limiting severely the final density of the sintered bodies

Table 2: Surface area (m^2/g) and mean particles diameter of the calcined samples.

Sample	Surface area (m^2/g)	Mean particles diameter (nm)
N-SDC20	95.4	8.8
T-SDC20	71.5	11.7
C-SDC20	51.5	16.3
U-SDC20	45.6	18.4

[14]. Furthermore, the detailed analysis of the larger particles reveals their quite dense structure very likely corresponding to hard agglomerates. Finally, the morphology of C-SDC20 sample shown in Figure 4(c) is similar to that pointed out for N-SDC20 and T-SDC20 although the clusters possess rounded shape and their structure does not appear dense.
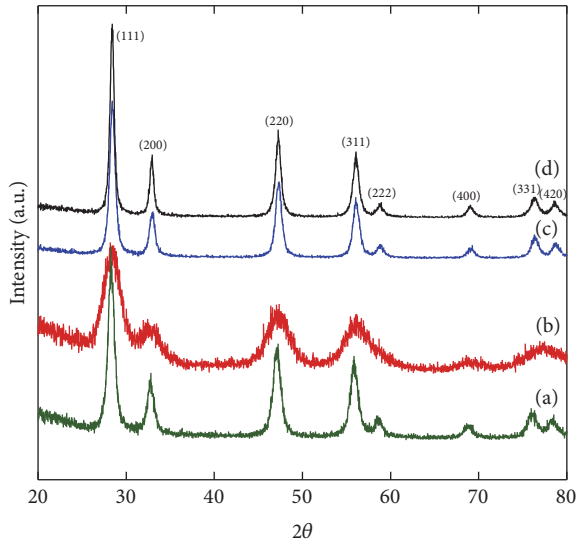
FIGURE 3: XRD patterns of the samples calcined at 600°C for 2 hours: N-SDC20 (a), T-SDC20 (b), C-SDC20 (c), and U-SDC20 (d).

TABLE 3: Relative density of the sintered pellets.

Sample	Relative density (%)
N-SDC20	83.5
T-SDC20	87.9
C-SDC20	98.4
U-SDC20	93.8

Very likely, the compaction for this sample is easier and the expected green density is significantly higher with respect to samples N-SDC20 and T-SDC20.

The calcined powders were uniaxially pressed and then sintered in air at 1500°C for 6 h. The apparent density was measured by Archimedes' balance and the results are reported in Table 3; relative density was estimated starting from real density reported before. The very different densification is clear and can be easily related to the calcined powders microstructure. Samples N-SDC20 and T-SDC20, which were characterized by the worst powders morphology, possess a relative density well below 90%. U-GDC20 specimen is densified in a satisfactory way, with a density next to 94%; C-SDC20 body appears very well densified with a relative density in excess to 98%.

The microstructure of sintered samples is reported in Figure 5. N-SDC20 and T-SDC20 specimens are characterized by a very heterogeneous microstructure; there are regions well densified and embedded in a very porous matrix characterized by very large and continuous porosity. Wider sintered regions appear in T-SDC20 samples, accounting for higher relative density (87.9% against 83.5%). Reported SEM micrographs confirm the hypotheses that hard agglomerates had been formed during the calcination step in samples N-SDC20 and T-SDC20. Bigger (hard agglomerates) and smaller particles cannot be well compacted upon pressing, resulting in very numerous internal flaws and limited green and final density.

In the case of U-SDC10 sample, the uniform morphology of the powders results in a very homogeneous microstructure in the sintered pellet (Figure 5(d)); some limited residual porosity (6.2%) is present and determined by very small (ca. 1 μm diameter) and homogeneously distributed pores. Such pores are probably the result of the intergranular porosity in the green specimen, which could not be completely closed during the sintering process.

Finally, the microstructure of C-SDC20 sample is shown in Figure 5(c); it is characterized by isometric and micrometric grains, well-developed straight grain boundaries; and very low porosity, thus confirming the very high relative density. This sample attained a nearly optimal densification with typical ceramic microstructure in the final stage of sintering.

Figure 6 shows additional SEM pictures for C-SDC20 and U-SDC20 samples that allow the evaluation of a grain size around 2 μm.

In order to analyze the sintering behavior of the powders, dilatometric tests were carried out on the different specimens. Although both C-SDC20 and U-SDC20 were characterized by an excellent densification (as shown in Figures 5(c) and 5(d)), the dilatometric curves referred to these specimens (Figure 7, plots (c) and (d) for C-SDC20 and U-SDC20, resp.) show very different features. At first, C-SDC20 is characterized by a much higher sintering shrinkage (nearly 25%), in agreement with the highest measured density after the sintering treatments. The shape of the two plots is also significantly different. The plot for U-SDC20 plot is more complex than for C-SDC20. U-SDC20 starts to shrink at ~650°C and a first sintering rate maximum is reached at 788°C. Then, sintering rate decreases reaching a minimum at 1110°C before increasing again up to 1550°C. The reasons of this "double" shrinkage phenomenon are not completely clear; nevertheless, it is significant to point out that the first starts at temperature slightly higher than the calcination temperature of the powder (600°C). Therefore, two possible explanations can be suggested. During the dilatometric test, the crystallization of some residual amorphous phase is activated at 650°C leading to a moderate shrinkage of the pressed pellet. Then, at higher temperature, proper densification phenomena are activated and they are responsible for the second shrinkage event. Alternatively, one can assume that the powders within the granules are partially sintered during the calcination process; when, during the dilatometric test, the temperature exceeds 600°C, nanometric intragranular pores start to close and the process is completed before 1100°C, leading to a first shrinkage event. The larger intergranular pores cannot be closed completely at such temperatures and their removal is responsible for the successive shrinkage, which is not completed up to 1550°C (as confirmed by SEM micrographs on the sintered samples).

The dilatometric plot (Figure 7(c)) for C-SDC20 sample is much more regular. The shrinkage is activated at temperatures lower than those recorded for U-SDC20 and the sintering rate shows only one maximum around 870°C. The densification phenomena are almost completed at 1300°C and the heating process up to 1550°C does not lead to particular additional advantages. This behavior could be related to better green specimen, characterized by homogeneous
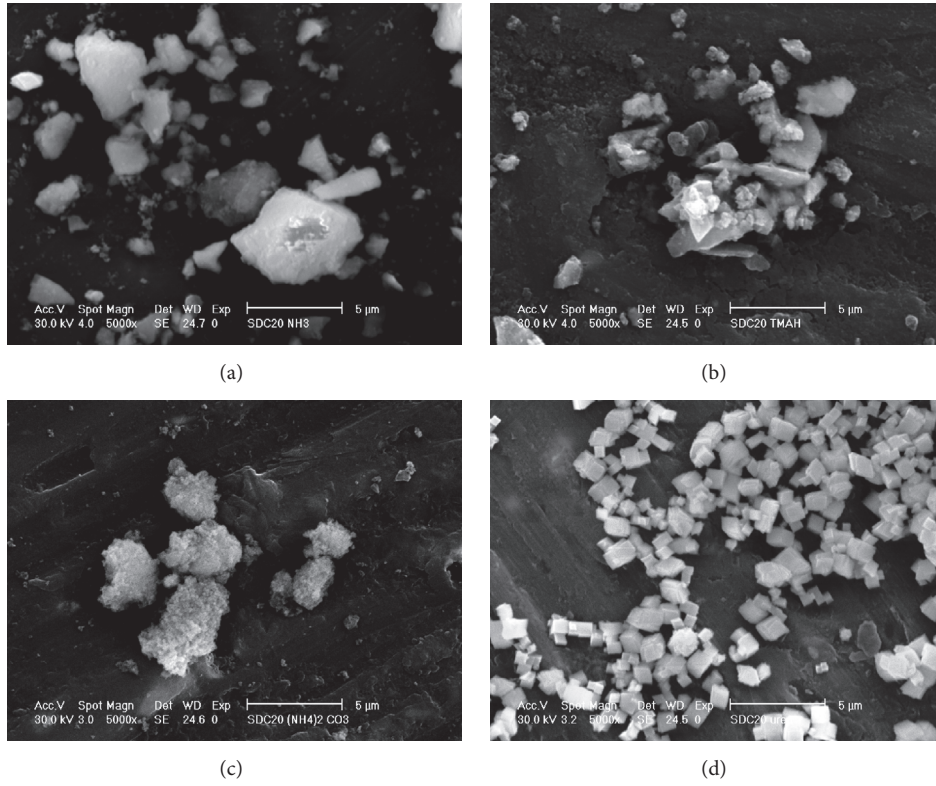
(a)

(b)

(c)

(d)

FIGURE 4: Morphology of the powder agglomerates after calcination: N-SDC20 (a), T-SDC20 (b), C-SDC20 (c), and U-SDC20 (d).
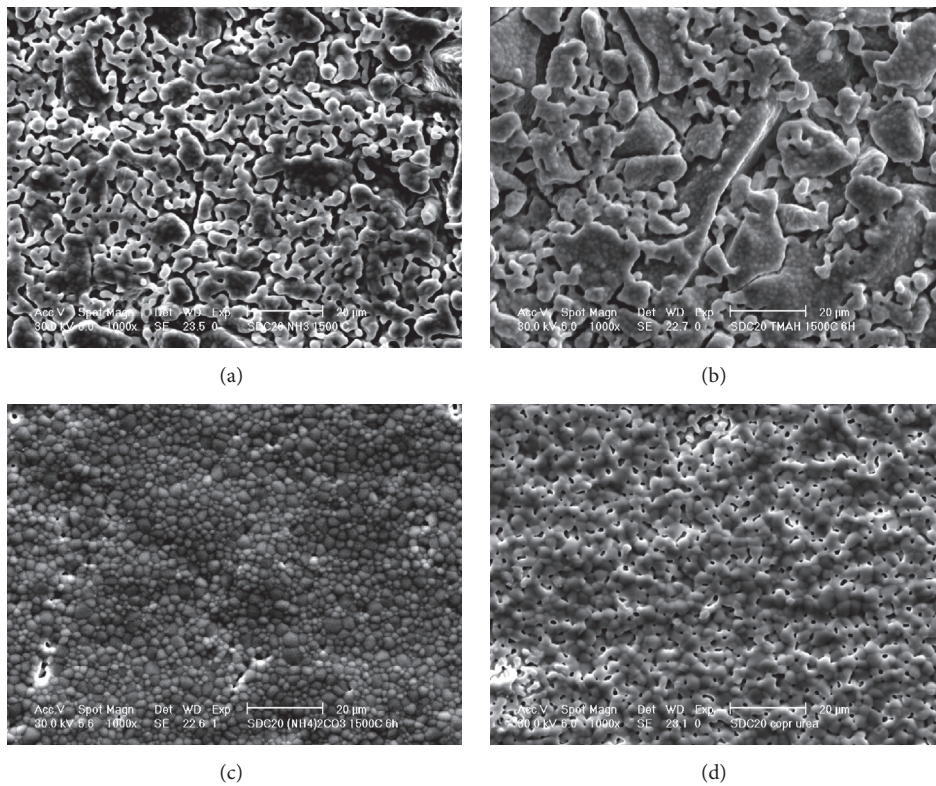

(a)

(b)

(c)

(d)

FIGURE 5: SEM micrographs of sintered pellets at low magnification (1000x): N-SDC20 (a), T-SDC20 (b), C-SDC20 (c), and U-SDC20 (d).
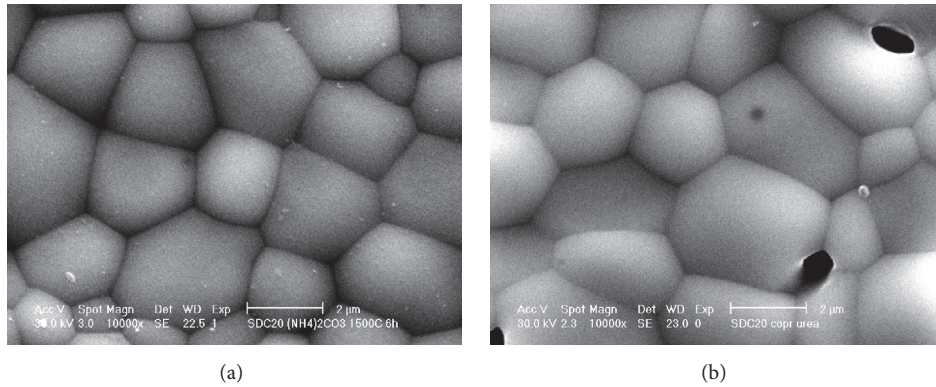
(a)

(b)

FIGURE 6: SEM micrographs of sintered pellets of samples C-SDC20 (a) and U-SDC20 (b) at high magnification.
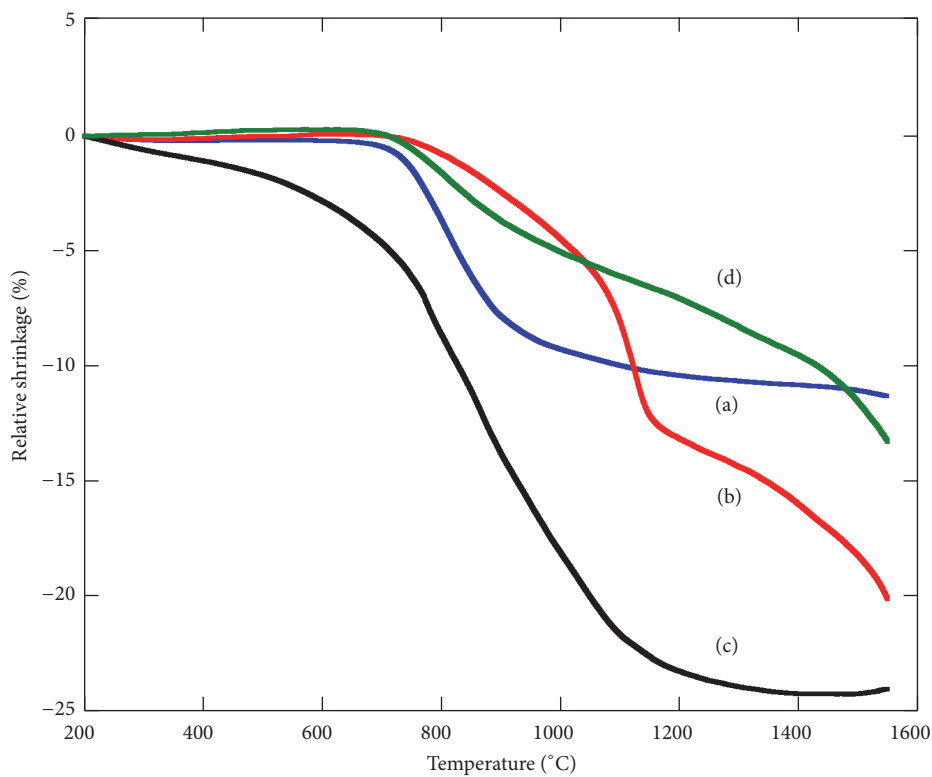

FIGURE 7: Linear shrinkage upon sintering for N-SDC20 (a), T-SDC20 (b), C-SDC20 (c), and U-SDC20 (d) powder.

nanometric porosity distribution and absence of coarse intergranular pores.

Interestingly, also for specimens characterized by poor densification upon sintering (Figures 5(a) and 5(b)), that is, T and N-SDC20, shrinkage is substantial. This is a clear evidence that the low density measured on the sintered specimens (Table 3) is a result of the low quality of the green bodies, rather than a nonefficient sintering process.

The dilatometric behavior of T-SDC20 (Figure 7(b)) is quite similar to that reported for U-SDC20, both powders showing a "double-shrinkage" curve. Nevertheless, T-SDC20 presents a first shrinkage much larger than that observed in the specimen treated with urea. This is likely related to

the fact that T-SDC20 powder was not well crystallized after calcination. Therefore, upon heating, the crystallization of a residual amorphous phase can be pointed out increasing the magnitude of the first shrinkage event. Conversely, the second shrinkage is associated with densification phenomena.

N-SDC20 shows one main shrinkage event starting at temperatures slightly higher than the calcination one (Figure 7(a)). This is probably related to a residual densification taking place within the granules and closing the nanometric porosity. A limited second shrinkage could be pointed out at high temperature (starting from ~1450°C) when the sintering rate slightly increases. This second event is probably related to some poor intergranular densification

mechanisms. The fact that the porosity between granules can be only very partially closed is coherent with the low density of N-SDC20 reported in Table 3.

4. Conclusions

Nanocrystalline 20 mol% samarium-doped ceria powders with fluorite structure were successfully synthesized in the present work by coprecipitation route using four different precipitating agents (NH_3, TMAH, $(NH_4)_2CO_3$, and urea) and successive calcination at 600°C for 2 h. The morphology of the produced powders is very different; the presence of hard agglomerates is undoubtedly revealed for powders obtained using ammonia and TMAH. Very different sintering behavior was also recorded on pellets realized by pressing the synthesized powders. The best densification behavior was observed for powders produced using $(NH_4)_2CO_3$ while those obtained using ammonia and TMAH lead always to the presence of significant residual porosity.

According to the results obtained here, it is possible to claim that in the case of samarium-doped ceria and, in general, in ceria-based ceramics, the use of precipitating agents which favors the direct formation of crystalline fluorite ceria leads to the formation of hard agglomerates after the calcination step. Therefore, for synthesizing these materials by coprecipitation route, precipitating agents which do not favor the direct crystallization of fluorite should be chosen and those based on carbonates appear a good choice.
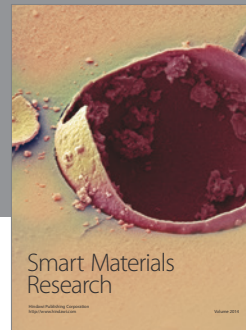
Competing Interests

The authors declare that they have no competing interests.

References

[1] C. Sun, H. Li, and L. Chen, "Nanostructured ceria-based materials: synthesis, properties, and applications," *Energy and Environmental Science*, vol. 5, no. 9, pp. 8475–8505, 2012.

[2] F. F. Muñoz, A. G. Leyva, R. T. Baker, and R. O. Fuentes, "Effect of preparation method on the properties of nanostructured gadolinia-doped ceria materials for IT-SOFCs," *International Journal of Hydrogen Energy*, vol. 37, no. 19, pp. 14854–14863, 2012.

[3] A. Arabaci and Ö. Serin, "Characterization of Sm-doped ceria ceramics synthesized by two different methods," *Journal of Materials Engineering and Performance*, vol. 24, no. 7, pp. 2730–2737, 2015.

[4] G. Accardo, C. Ferone, R. Cioffi, D. Frattini, L. Spiridigliozzi, and G. Dell'Agli, "Electrical and microstructural characterization of Ceramic Gadolinium doped Ceria Electrolytes for ITSOFCs by sol-gel route," *Journal of Applied Biomaterials & Functional Materials*, vol. 14, no. 1, pp. e35–e41, 2016.

[5] G. Dell'Agli, L. Spiridigliozzi, A. Marocco, G. Accardo, C. Ferone, and R. Cioffi, "Effect of the mineralizer solution in the hydrothermal synthesis of Gadolinium-doped (10% mol Gd) ceria nanopowders," *Journal of Applied Biomaterials & Functional Materials*, vol. 14, no. 2, pp. e189–e196, 2016.

[6] A. Arabaci, "Synthesis and crystal kinetics of cerium oxide nanocrystallites prepared by co-precipitation process," *Ceramics International*, vol. 41, no. 4, pp. 5836–5842, 2015.

[7] N. Jaiswal, B. Gupta, D. Kumar, and O. Parkash, "Effect of addition of erbium stabilized bismuth oxide on the conductivity of lanthanum doped ceria solid electrolyte for IT-SOFCs," *Journal of Alloys and Compounds*, vol. 633, pp. 174–182, 2015.

[8] S. Kuharuangrong, "Ionic conductivity of Sm, Gd, Dy and Er-doped ceria," *Journal of Power Sources*, vol. 171, no. 2, pp. 506–510, 2007.

[9] C. Veranitisagul, A. Kaewvilai, W. Wattanathana, N. Koonsaeng, E. Traversa, and A. Laobuthee, "Electrolyte materials for solid oxide fuel cells derived from metal complexes: Gadolinia-doped ceria," *Ceramics International*, vol. 38, no. 3, pp. 2403–2409, 2012.

[10] L. Spiridigliozzi, G. Dell'Agli, A. Marocco, G. Accardo, C. Ferone, and R. Cioffi, "Hydrothermal synthesis at low temperature of gadolinium-doped ceria," in *Proceedings of the 6th European Fuel Cell*, Naples, Italy, December 2015.

[11] M. Biesuz, G. Dell'Agli, L. Spiridigliozzi, C. Ferone, and V. Sglavo, "Conventional and field-assisted sintering of nanosized Gd-doped ceria synthesized by co-precipitation," *Ceramics International*, vol. 42, no. 10, pp. 11766–11771, 2016.

[12] D. Segal, "Chemical synthesis of ceramic materials," *Journal of Materials Chemistry*, vol. 7, no. 8, pp. 1297–1305, 1997.

[13] B. D. Cullity, *Elements of X-Rays Diffraction*, Addison-Wesley, New York, NY, USA, 2nd edition, 1978.

[14] M. N. Rahaman, *Ceramics Processing*, Taylor & Francis, New York, NY, USA, 2007.

[15] C. J. Shih, Y. J. Chen, and M. H. Hon, "Synthesis and crystal kinetics of cerium oxide nanocrystallites prepared by co-precipitation process," *Materials Chemistry and Physics*, vol. 121, no. 1-2, pp. 99–102, 2010.

[16] Y. X. Li, X. Z. Zhou, Y. Wang, and X. Z. You, "Preparation of nano-sized CeO_2 by mechanochemical reaction of cerium carbonate with sodium hydroxide," *Materials Letters*, vol. 58, no. 1-2, pp. 245–249, 2004.

[17] J.-G. Li, T. Ikegami, Y. Wang, and T. Mori, "Reactive ceria nanopowders via carbonate precipitation," *Journal of the American Ceramic Society*, vol. 85, no. 9, pp. 2376–2378, 2002.

[18] C. Suryanarayana and M. G. Norton, *X-Ray Diffraction: A Practical Approach*, Springer, 1998.

[19] G. Dell'Agli and G. Mascolo, "Sinterability of 8Y-ZrO_2 powders hydrothermally synthesized at low temperature," *Solid State Ionics*, vol. 160, no. 3-4, pp. 363–371, 2003.

[20] G. Dell'Agli, G. Mascolo, M. C. Mascolo, and C. Pagliuca, "Crystallization-stabilization mechanism of yttria-doped zirconia by hydrothermal treatment of mechanical mixtures of zirconia xerogel and crystalline yttria," *Journal of Crystal Growth*, vol. 280, no. 1-2, pp. 255–265, 2005.

[21] E. C. C. Souza and E. N. S. Muccillo, "Effect of solvent on physical properties of samaria-doped ceria prepared by homogeneous precipitation," *Journal of Alloys and Compounds*, vol. 473, no. 1-2, pp. 560–566, 2009.

[22] G. Dell'Agli, C. Ferone, G. Mascolo, and M. Pansini, "Crystallization of monoclinic zirconia from metastable phases," *Solid State Ionics*, vol. 127, no. 3, pp. 223–230, 2000.